J. Adv. Model. Earth Syst., **Vol. 2**, Art. #13, 17 pp.

# Atmospheric Dynamics of Earth-Like Tidally Locked Aquaplanets

*Timothy M. Merlis and Tapio Schneider*

California Institute of Technology, Pasadena, California

Manuscript submitted 26 January 2010; in final form 14 June 2010

We present simulations of atmospheres of Earth-like aquaplanets that are tidally locked to their star, that is, planets whose orbital period is equal to the rotation period about their spin axis, so that one side always faces the star and the other side is always dark. Such simulations are of interest in the study of tidally locked terrestrial exoplanets and as illustrations of how planetary rotation and the insolation distribution shape climate. As extreme cases illustrating the effects of slow and rapid rotation, we consider planets with rotation periods equal to one current Earth year and one current Earth day. The dynamics responsible for the surface climate (e.g., winds, temperature, precipitation) and the general circulation of the atmosphere are discussed in light of existing theories of atmospheric circulations. For example, as expected from the increasing importance of Coriolis accelerations relative to inertial accelerations as the rotation rate increases, the winds are approximately isotropic and divergent at leading order in the slowly rotating atmosphere but are predominantly zonal and rotational in the rapidly rotating atmosphere. Free-atmospheric horizontal temperature variations in the slowly rotating atmosphere are generally weaker than in the rapidly rotating atmosphere. Interestingly, the surface temperature on the night side of the planets does not fall below ~240 K in either the rapidly or slowly rotating atmosphere; that is, heat transport from the day side to the night side of the planets efficiently reduces temperature contrasts in either case. Rotational waves and eddies shape the distribution of winds, temperature, and precipitation in the rapidly rotating atmosphere; in the slowly rotating atmosphere, these distributions are controlled by simpler divergent circulations. Both the slowly and rapidly rotating atmospheres exhibit equatorial superrotation. Systematic variation of the planetary rotation rate shows that the equatorial superrotation varies non-monotonically with rotation rate, whereas the surface temperature contrast between the day side and the night side does not vary strongly with changes in rotation rate.

DOI:10.3894/JAMES.2010.2.13

## 1. Introduction

Planets generally evolve toward a state in which they become tidally locked to their star. Torques the star exerts on tidal bulges on a planet lead to an exchange between the spin angular momentum of the planetary rotation and orbital angular momentum of the planet's revolution around the star, such that the rotation period around the spin axis gradually approaches the orbital period of the planet (Hubbard 1984). (The spin angular momentum of the star may also participate in this angular momentum exchange.) This process reaches its tidally locked end state when the rotation period is equal to the orbital period, so that one side of the planet always faces the star and the other side is always dark. The time it takes to reach this end state may exceed the lifetime of the planetary system, so it may never be reached (this is the case for the Sun-Earth system). But planets that are close to their star can reach a tidally locked state more quickly. Such close planets in other solar systems are easier to detect than planets farther away from their star, and exoplanets that are believed to be tidally locked have indeed been detected in recent years (e.g., Charbonneau et al. 2000). Here we investigate the atmospheric dynamics of Earth-like tidally locked aquaplanets through simulations with a three-dimensional general circulation model (GCM). Our purpose is pedagogic: we contrast rapidly and slowly rotating tidally locked Earth-like planets with each other and with Earth itself to illustrate the extent to which atmospheric dynamics depend on the insolation distribution and planetary rotation rate.

**To whom correspondence should be addressed.**
Timothy M. Merlis, 1200 E. California Blvd. MC 100-23, Pasadena, CA 91125, USA
tmerlis@caltech.edu

There are two areas of existing research on the atmospheric dynamics of tidally locked planets. First, there are several studies motivated by "hot Jupiters"—large, close-in planets that have been observed transiting a star (see Showman et al. (2010) for a review). Second, there are studies of Earth-like exoplanets closely orbiting a relatively cool star—planets that have not yet been but may be detected soon, for example, by NASA's recently launched *Kepler* space telescope or by groundbased telescopes (as demonstrated by the recent discoveries of Charbonneau et al. (2009)). Joshi et al. (1997) investigated the large-scale circulation of such Earth-like planets and explored how their climate depends on the mass of the atmosphere. And Joshi (2003) documented their hydrological cycle using an Earth climate model.

The studies by Joshi et al. provide a description of Earth-like tidally locked atmospheric circulations and how they depend on some parameters, such as the atmospheric mass. But some questions remain, among them: (i) How does the planet's rotation rate affect the circulation and climate? (ii) What controls the precipitation distribution (location of convergence zones)? (iii) What mechanisms generate large-scale features of the circulation, such as jets? (iv) What determines the atmospheric stratification?

We address these questions by simulating tidally locked Earth-like aquaplanets. We focus on simulations with rotation periods equal to one current Earth year and one current Earth day as two illustrative cases: The slowly rotating case corresponds roughly to the tidally locked end state Earth would reach if the Sun were not changing, that is, if the solar constant $S_0 = 1367\ \mathrm{Wm}^{-2}$ remained fixed. The rapidly rotating case corresponds to a terrestrial planet sufficiently close to a cool host star, so that the orbital period is one Earth day but the average insolation reaching the planet still is $S_0 = 1367\ \mathrm{Wm}^{-2}$, as presently on Earth. Additionally, we explore more systematically how some characteristics—such as equatorial superrotation—depend on the planetary rotation rate.

## 2. General Circulation Model

We use an idealized atmosphere GCM with an active hydrological cycle and an aquaplanet (slab ocean) lower boundary condition. The slab ocean has the heat capacity of 5 m of water and has no explicit horizontal transports but is implicitly assumed to transport water from regions of net precipitation to regions of net evaporation, so that the local water supply is unlimited. The GCM is a modified version of the model described in O'Gorman and Schneider (2008), which is similar to the model described in Frierson et al. (2006). Briefly, the GCM is a three-dimensional primitive-equation model of an ideal-gas atmosphere. It uses the spectral transform method in the horizontal, with resolution T85, and finite differences in $\sigma = p/p_s$ coordinates (pressure $p$ and surface pressure $p_s$) in the vertical, with 30 unequally spaced levels; the time step is 200 s. Subgrid-scale dissipation is represented by an exponential cutoff filter (Smith et al. 2002), which acts on spherical wavenumbers greater than 40, with a damping timescale of 1 h on the smallest resolved scale. Most features of the simulated flows are similar at T42 resolution or with different subgrid-scale filters; exceptions are noted below.

The GCM has a surface with uniform albedo (0.38) and uniform roughness lengths for momentum fluxes ($5 \times 10^{-3}$ m) and for latent and sensible heat fluxes ($10^{-5}$ m). It has a gray radiation scheme and a quasi-equilibrium moist convection scheme that relaxes convectively unstable atmospheric columns to a moist pseudo-adiabat with constant (70%) relative humidity (Frierson 2007). Only the vapor-liquid phase transition is taken into account, and the latent heat of vaporization is taken to be constant. No liquid water is retained in the atmosphere, so any precipitation that forms immediately falls to the surface. Radiative effects of clouds are not taken into account, except insofar as the surface albedo and radiative parameters are chosen to mimic some of the global-mean effects of clouds on Earth's radiative budgets.

Other model details can be found in O'Gorman and Schneider (2008). However, the radiation scheme differs from that in O'Gorman and Schneider (2008) and is described in what follows.

### 2.1. Tidally locked insolation

The top-of-atmosphere insolation is held fixed at the instantaneous value for a spherical planet (e.g., Hartmann 1994),

$$S_{\mathrm{TOA}} = S_0 \times \max(0, \cos(\phi)\cos(\lambda - \lambda_0)), \qquad (2.1)$$

where $\phi$ is latitude and $\lambda$ is longitude, with subsolar longitude $\lambda_0 = 270°$ and solar constant $S_0 = 1367\ \mathrm{Wm}^{-2}$. There is no diurnal cycle of insolation. That is, we assume zero eccentricity of the orbit and zero obliquity of the spin axis.

Absorption of solar radiation in the atmosphere is represented by attenuation of the downward flux of radiation with an optical depth that varies quadratically with pressure, so that

$$S(p) = S_{\mathrm{TOA}} \exp\left[-\left(\frac{p}{p_0}\right)^2\right] \qquad (2.2)$$

with $p_0 = 10^5$ Pa.

### 2.2. Longwave optical depth

O'Gorman and Schneider (2008) used a gray radiation scheme with a longwave optical depth that was uniform in longitude and a prescribed function of latitude, thereby ignoring any longwave water vapor feedback. This is not adequate for tidally locked simulations in which the water vapor concentration varies strongly with longitude. Therefore, we use a longwave optical depth that varies with the local water vapor concentration (cf. Thuburn and Craig 2000), providing a crude representation of longwave water vapor feedback.

As in Frierson et al. (2006), the longwave optical depth $\tau$ has a term linear in pressure $p$, representing well-mixed absorbers like $CO_2$, and a term quartic in pressure, representing water vapor, an absorber with a scale height that is one quarter of the pressure scale height,

$$\tau = \tau_0 \left(\frac{p}{p_0}\right)^4 + \tau_1 \left(\frac{p}{p_0}\right). \tag{2.3}$$

Here, $\tau_1 = 1.2$ and $p_0 = 10^5$ Pa are constants. The optical thickness $\tau_0$ is a function of the model's instantaneous column water vapor concentration,

$$\tau_0 = \frac{1}{p_1}\int_0^{p_s} r\, dp, \tag{2.4}$$

with water vapor mixing ratio $r$ and an empirical constant $p_1 = 98$ Pa to keep $\tau_0$ order one for conditions typical of Earth.

We have also run simulations in which the absorptivity of the absorber representing water vapor depended locally on the specific humidity on each model level. The details of the radiation scheme such as the constants chosen and the exact dependence of the optical depth on the water vapor concentration affected quantitative aspects of the simulations (e.g., the precise surface temperatures obtained), but not the large-scale dynamics on which we focus. With or without a vertically-local dependence of absorptivity on the water vapor concentration, the simulated surface climate is similar to those presented in Joshi (2003), who used a more complete representation of radiation including radiative effects of clouds. This gives us confidence that the qualitative results presented here do not depend on the details of the radiation scheme.

### 2.3. Simulations

We conducted a rapidly rotating simulation with planetary rotation rate equal to that of present-day Earth, $\Omega = \Omega_E = 7.292 \times 10^{-5}$ s$^{-1}$, and a slowly rotating simulation with planetary rotation rate approximately equal to one present-day Earth year, $\Omega = \Omega_E/365$. The results we present are averages over the last 500 days of 4000-day simulations (with 1 day = 86400 s, irrespective of the planetary rotation rate). During the first 3000 days of the simulation, we adjusted the subgrid-scale dissipation parameters to the values stated above to ensure there was no energy build-up at the smallest resolved scales. The slowly rotating simulation is presented in section 3, and the rapidly rotating simulation is presented in section 4.

Additionally, we conducted simulations with intermediate rotation rates, to explore how equatorial superrotation and the day-side to night-side surface temperature contrast depend on the rotation rate. The last 500 days of 2000-day simulations are presented in section 5.

## 3. Slowly Rotating Simulation

The Rossby number $\mathrm{Ro} = U/(fL)$, with horizontal velocity scale $U$, Coriolis parameter $f$, and length scale $L$, is a measure of the importance of inertial accelerations ($\sim U^2/L$) relative to Coriolis accelerations ($\sim fU$) in the horizontal momentum equations. In rapidly rotating atmospheres, including Earth's, the Rossby number in the extratropics is small, and the dominant balance is geostrophic, that is, between pressure gradient forces and Coriolis forces. In slowly rotating atmospheres, the Rossby number may not be small. If $\mathrm{Ro} = O(1)$, inertial and Coriolis accelerations both are important, as in the deep tropics of Earth's atmosphere. If $\mathrm{Ro} \gg 1$, Coriolis accelerations and effects of planetary rotation become unimportant. In that case, there is no distinguished direction in the horizontal momentum equations, so the horizontal flow is expected to be isotropic, that is, the zonal velocity scale $U$ and meridional velocity scale $V$ are of the same order. This is the dynamical regime of our slowly rotating simulation.

In this dynamical regime, the magnitude of horizontal temperature variations can be estimated through scale analysis of the horizontal momentum equations (Charney 1963). In the free atmosphere, where frictional forces can be neglected, inertial accelerations scale advectively, like $\sim U^2/L$, and are balanced by accelerations owing to pressure gradients, which scale like $\delta p/(\rho L)$, where $\delta p$ is the scale of horizontal pressure variations and $\rho$ is density. The density and vertical pressure variations are related by the hydrostatic relation, $p/H \sim \rho g$, where $H = RT/g$ is the pressure scale height (specific gas constant $R$ and temperature $T$). If one combines the scalings from the horizontal momentum and hydrostatic equations, horizontal variations in pressure, density, and (potential) temperature (using the ideal gas law) scale like

$$\frac{\delta p}{p} \sim \frac{\delta \rho}{\rho} \sim \frac{\delta \theta}{\theta} \sim \frac{U^2}{gH} \equiv \mathrm{Fr}, \tag{3.1}$$

where $\mathrm{Fr} = U^2/(gH)$ is the Froude number. For a terrestrial planet with $H \approx 7$ km and $g = 9.8$ m s$^{-2}$, the Froude number is $\mathrm{Fr} \lesssim 10^{-2}$ for velocities $U \lesssim 25$ m s$^{-1}$. So free-atmospheric horizontal temperature and pressure variations are expected to be small insofar as velocities are not too strong (e.g., if their magnitude is limited by shear instabilities). This is the case in the tropics of Earth's atmosphere, and these expectations are also borne out in the slowly rotating simulation.

### 3.1. Surface temperature and outgoing longwave radiation

In the slowly rotating simulation, the surface temperature mimics the insolation distribution on the day side of the planet, decreasing monotonically and isotropically away from the subsolar point; the night side of the planet has a nearly uniform surface temperature (Fig. 1). Though the surface temperature resembles the insolation distribution, the influence of atmospheric dynamics is clearly evident in that the night side of the planet is considerably warmer than the radiative-convective equilibrium temperature of 0 K.

For exoplanets, the outgoing longwave radiation (OLR) is more easily measurable than the surface temperature. In the

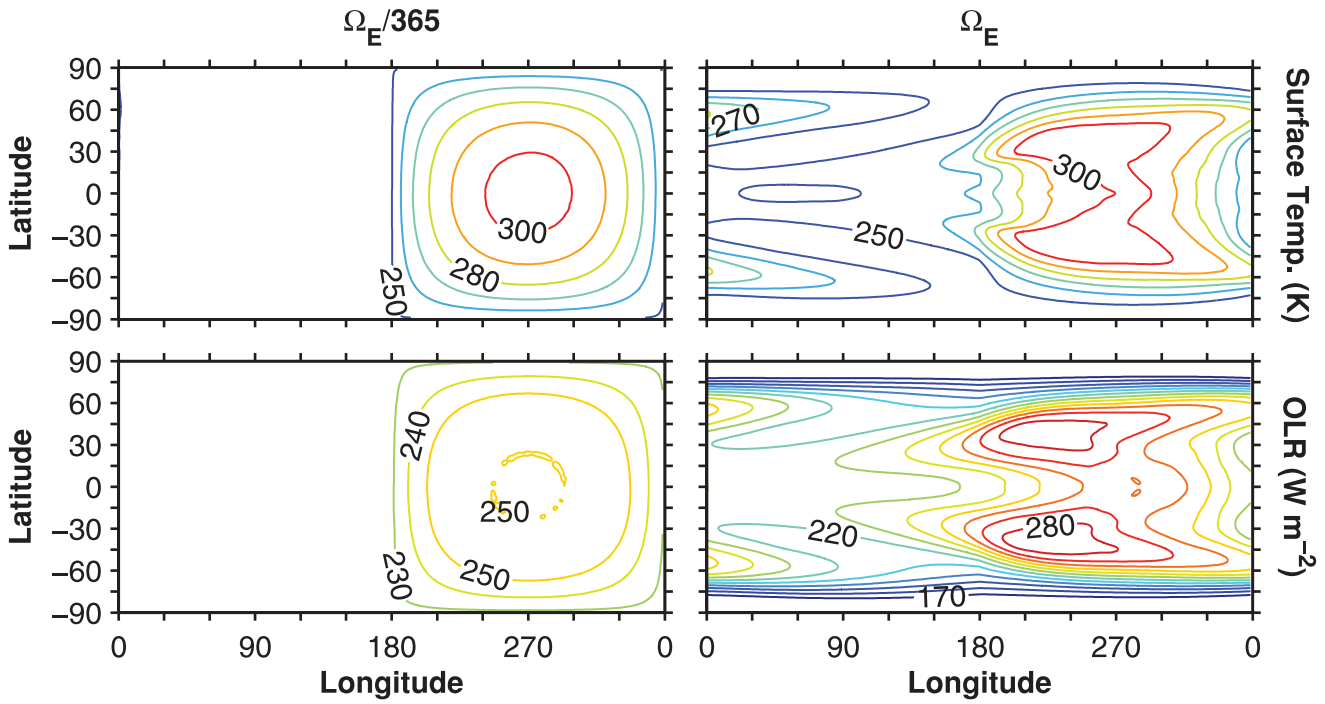


**Figure 1.** Top row: surface temperature (K) in simulations with $\Omega_E/365$ (left) and $\Omega_E$ (right). The contour interval is 10 K. Bottom row: outgoing longwave radiation, OLR, (W m$^{-2}$) in simulations with $\Omega_E/365$ (left) and $\Omega_E$ (right). The contour interval is 10 W m$^{-2}$.

slowly rotating simulation, the relative magnitude of the OLR contrast between the day side and night side of the planet is muted compared with that of the surface temperature contrast (Fig. 1) because free-tropospheric temperature gradients are weaker than surface temperature gradients (as will be discussed further in section 3d).

### 3.2. Hydrological cycle

Surface evaporation rates likewise mimic the insolation distribution (Fig. 2), as would be expected from a surface energy budget in which the dominant balance is between heating by shortwave radiation and cooling by evaporation. This is the dominant balance over oceans on Earth (e.g., Trenberth et al. 2009), and in general on sufficiently warm Earth-like aquaplanets (Pierrehumbert 2002; O'Gorman and Schneider 2008). The dominance of evaporation in the surface energy budget in sufficiently warm climates can be understood by considering how the Bowen ratio, the ratio of sensible to latent surface fluxes, depends on temperature. For surface fluxes given by bulk aerodynamic formulas, the Bowen ratio $B$ depends on the surface temperature $T_s$, the near-surface air temperature $T_a$, and the near-surface relative humidity $\mathcal{H}$,

$$B \sim \frac{c_p(T_s - T_a)}{L(q^*(T_s) - \mathcal{H}q^*(T_a))}, \tag{3.2}$$

where $q^*$ is the saturation specific humidity, $c_p$ is the specific heat of air at constant pressure, and $L$ is the latent heat of vaporization. Figure 3 shows the Bowen ratio as a function of surface temperature, assuming a fixed surface–air temperature difference and fixed relative humidity. We have fixed these to values that are representative of the GCM simulations for simplicity, but the surface–air temperature difference and relative humidity are not fixed in the GCM. For surface temperatures greater than ~290 K, latent heat fluxes are a factor of $\gtrsim$ 4 larger than sensible heat fluxes, as at Earth's surface (Trenberth et al. 2009). Similar arguments apply for net longwave radiative fluxes at the surface, which become small as the longwave optical thickness of the atmosphere and with it surface temperatures increase; see Pierrehumbert (2010) for a more complete discussion of the surface energy budget.

The precipitation rates likewise mimic the insolation distribution (Fig. 2). There is a convergence zone with large precipitation rates ($\geqslant$ 40 mm/day) around the subsolar point. Precipitation rates exceed evaporation rates within ~15° of the subsolar point. Outside that region on the day side, evaporation rates exceed precipitation rates (Fig. 2), which would lead to the generation of deserts there if the surface water supply were limited. The atmospheric circulation that gives rise to the moisture transport toward the subsolar point is discussed next.

### 3.3. General circulation of the atmosphere

The winds are approximately isotropic and divergent at leading order. They form a thermally direct overturning

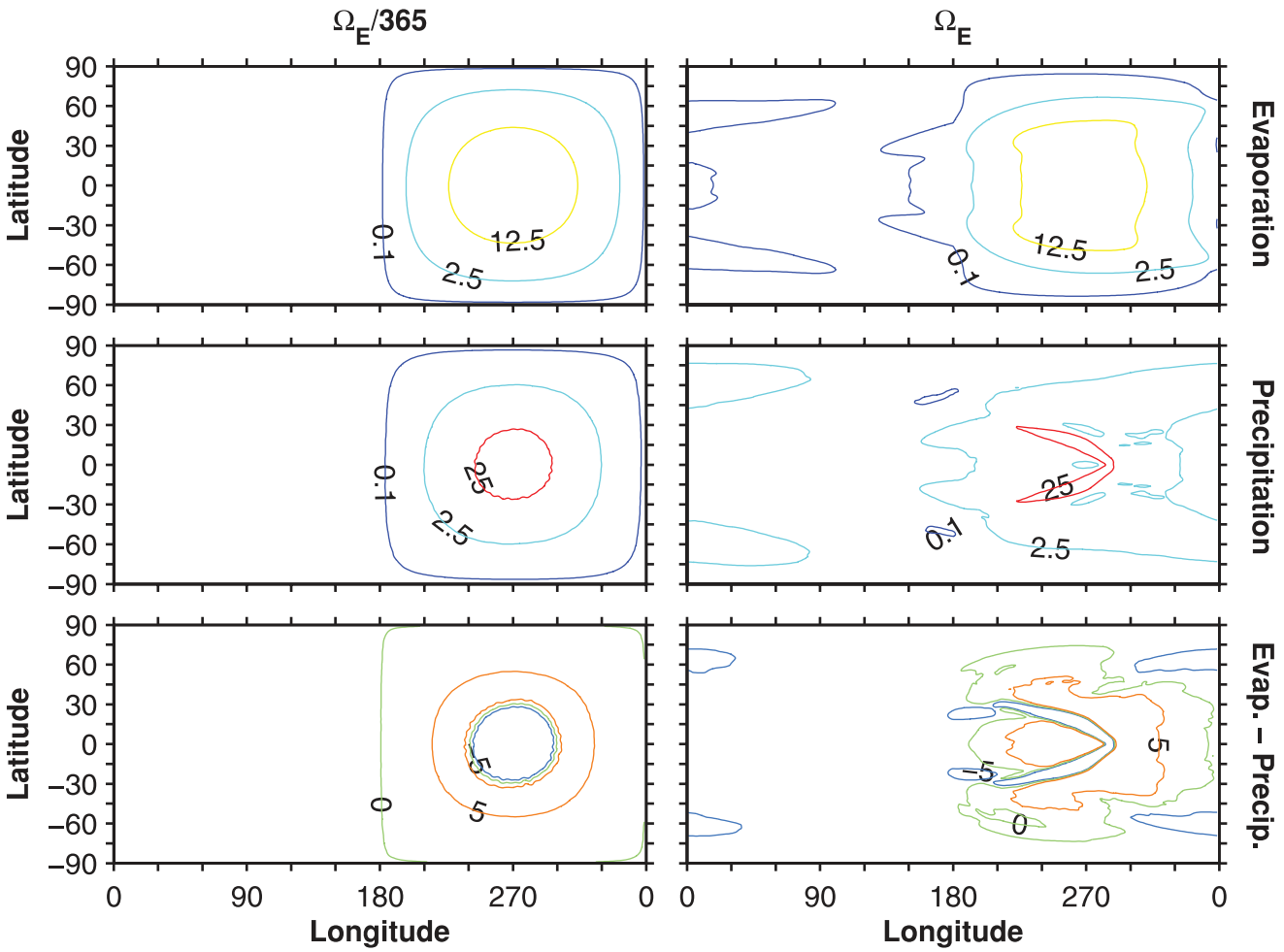


**Figure 2.** Evaporation (top row, mm day$^{-1}$), precipitation (middle row, mm day$^{-1}$), and evaporation minus precipitation (bottom row, mm day$^{-1}$) in simulations with $\Omega_E/365$ (left) and $\Omega_E$ (right). Contours are shown at 0.1, 2.5, and 12.5 mm day$^{-1}$ for evaporation, 0.1, 2.5, and 25.0 mm day$^{-1}$ for precipitation, and −5.0, 0, and 5.0 mm day$^{-1}$ for evaporation minus precipitation.

circulation, with lower-level convergence near the subsolar point, upper-level divergence above it, and weaker flow in between (Fig. 4). As in the simulations of Joshi et al. (1997),

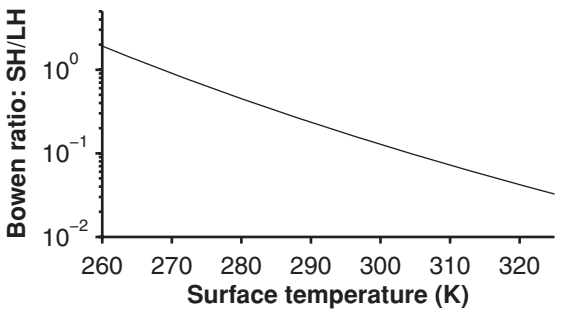


**Figure 3.** Bowen ratio vs surface temperature assuming a 3-K surface–air temperature difference, 70% relative humidity, and surface and surface air pressure of $10^5$ Pa, using the same simplified saturation vapor pressure formula as in the GCM.

the meridional surface flow crosses the poles. Moist convection in the vicinity of the subsolar point results in strong mean ascent in the mid-troposphere there; elsewhere there is weak subsidence associated with radiative cooling (Fig. 5). Consistent with the predominance of divergent and approximately isotropic flow, the Rossby number is large even in the extratropics (Ro $\gtrsim$ 10).

The zonal-mean zonal wind and streamfunction are shown in Fig. 6. The zonal-mean zonal wind is a weak residual of the opposing contributions from different longitudes (Fig. 4). In the upper troposphere near the equator, there are weak westerly (superrotating) zonal winds, as well as the eddy angular momentum flux convergence that, according to Hide's theorem, is necessary to sustain them (e.g., Hide 1969; Schneider 1977; Held and Hou 1980; Schneider 2006).

The Eulerian mean mass streamfunction consists of a Hadley cell in each hemisphere, which is a factor ~3 stronger than Earth's and extends essentially to the pole. These Hadley cells are thermodynamically direct circula-

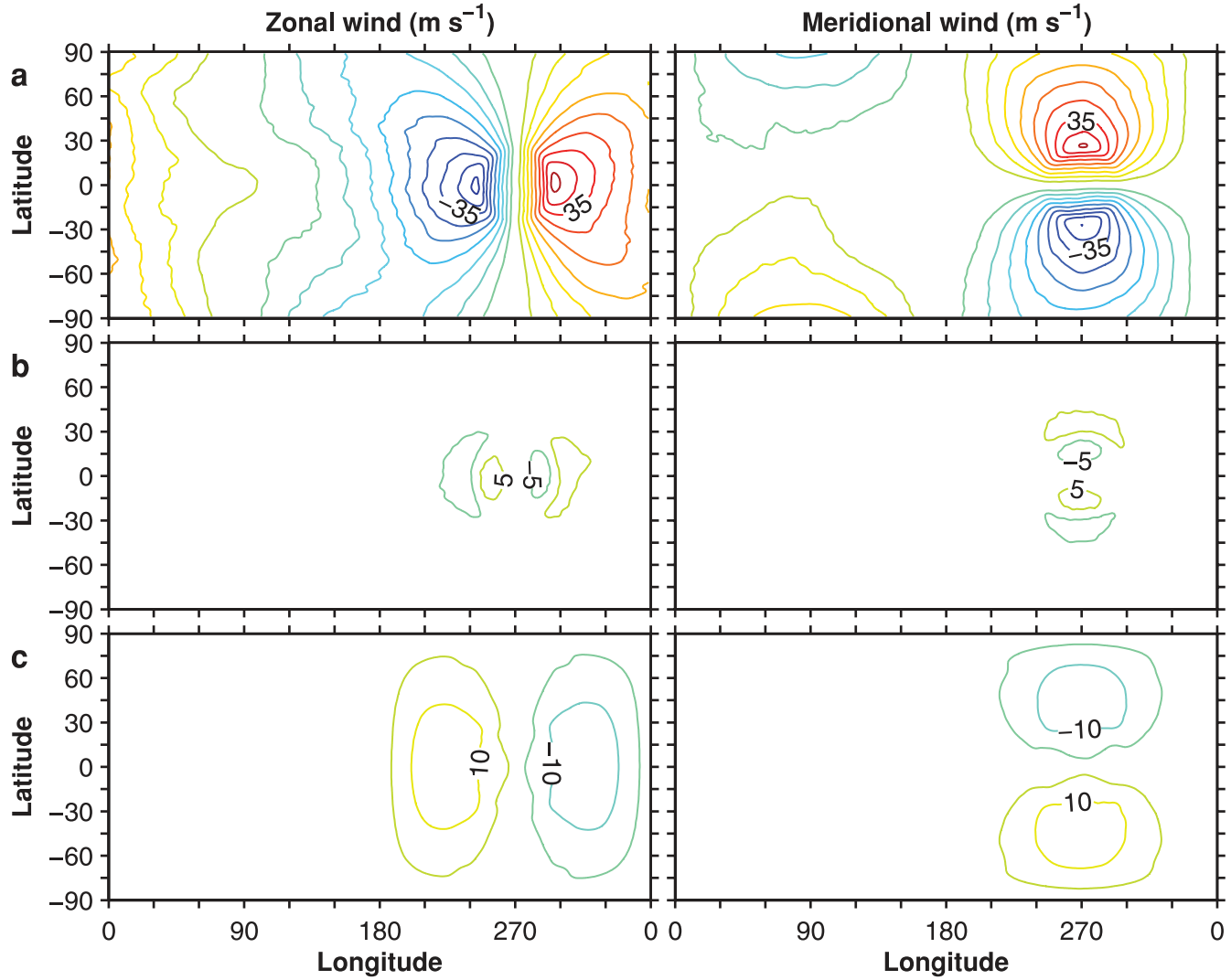


**Figure 4.** Zonal wind (left) and meridional wind (right) in $\Omega_E/365$ simulation on the $\sigma = 0.28$ (a), 0.54 (b), and 1.0 (c) surfaces. The contour interval is 5 m s$^{-1}$, and the zero contour is not shown.

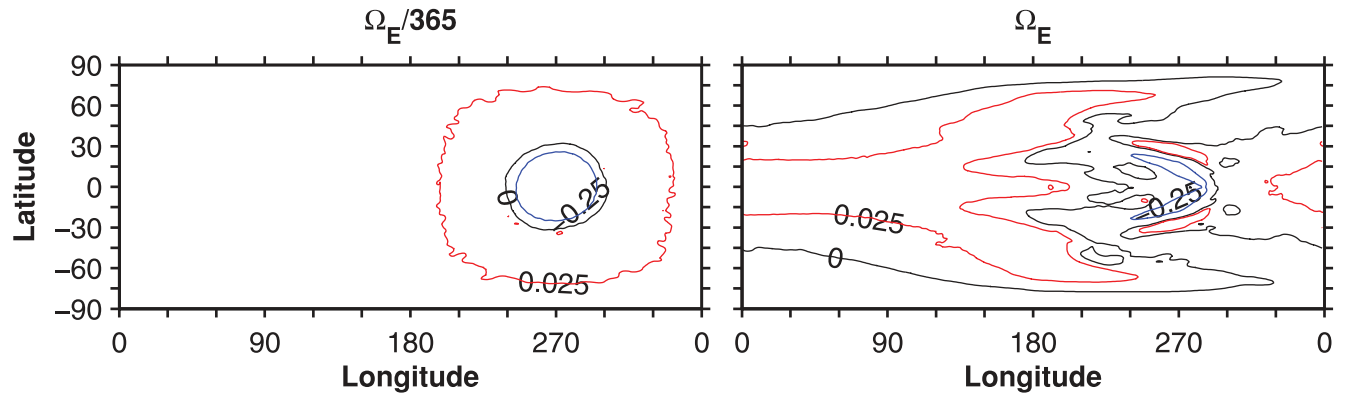


**Figure 5.** Pressure velocity ($\omega = Dp/Dt$) on the $\sigma = 0.54$ surface in simulations with $\Omega_E/365$ (left) and $\Omega_E$ (right). Contours are shown at −0.25 (blue), 0 (black), and 0.025 (red) Pa s$^{-1}$.

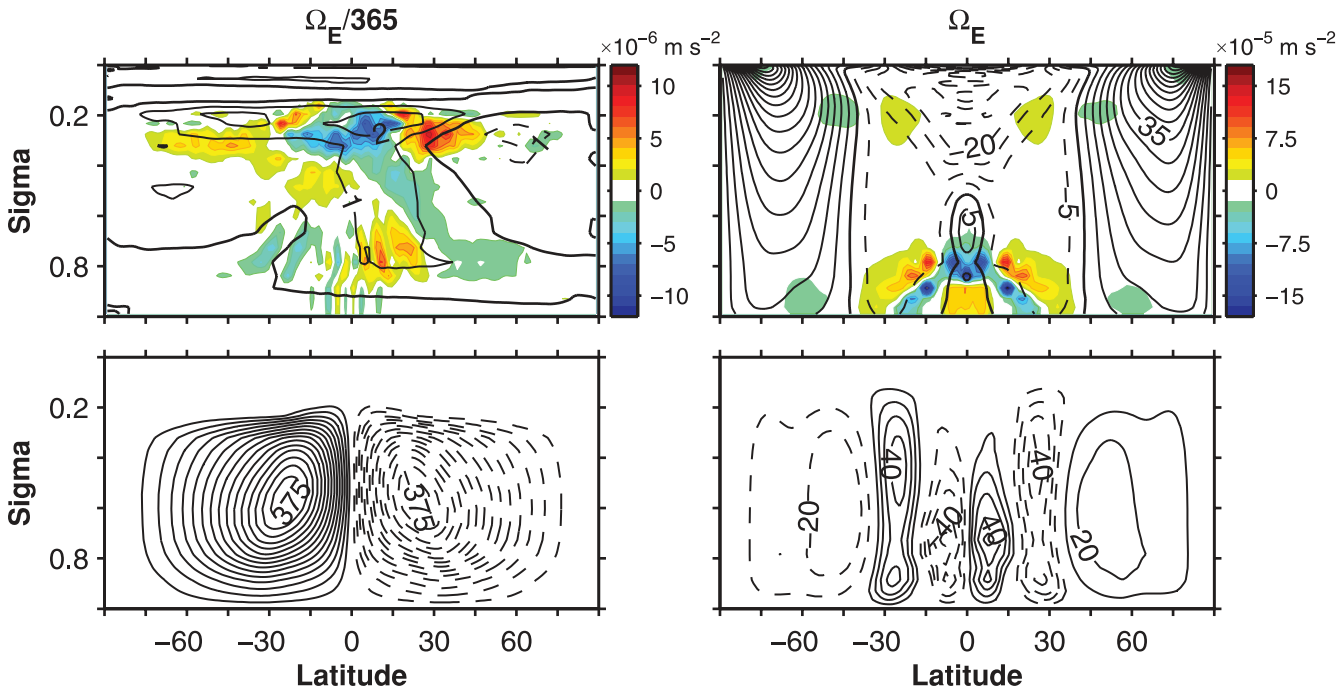


**Figure 6.** Circulation in simulations with $\Omega_E/365$ (left panels) and $\Omega_E$ (right panels). Top row: zonal-mean zonal wind (lines, contour interval 1 m s$^{-1}$ for $\Omega_E$ and 5 m s$^{-1}$ for $\Omega_E/365$) and divergence of the horizontal component of eddy (transient and stationary) angular momentum fluxes (colors, contour interval 1.0 × 10$^{-6}$ m s$^{-2}$ for $\Omega_E/365$ and 1.5 × 10$^{-5}$ m s$^{-2}$ for $\Omega_E$). Bottom row: Eulerian mean mass flux streamfunction (contour interval 25 × 10$^9$ kg s$^{-1}$ for $\Omega_E/365$ and 10 × 10$^9$ kg s$^{-1}$ for $\Omega_E$).

tions: the poleward flow to higher latitudes has larger moist static energy ($h = c_pT + gz + Lq$) than the near-surface return flow. The classic theory of Hadley cells with nearly inviscid, angular momentum-conserving upper branches predicts that the Hadley cell extent increases as the rotation rate decreases (Schneider 1977; Held and Hou 1980). However, the results of this theory do not strictly apply here because several assumptions on which it is based are violated. For example, the surface wind is not weak relative to the upper-tropospheric winds (Fig. 4), and the zonal wind is not in (geostrophic or gradient-wind) balance with meridional geopotential gradients (i.e., the meridional wind is not negligible in the meridional momentum equation). Nonetheless, it is to be expected that Hadley cells in slowly rotating atmospheres span hemispheres (Williams 1988).

The instantaneous, upper-tropospheric zonal wind is shown in Fig. 7, and a corresponding animation is available at doi: 10.3894/JAMES.2010.2.13.S1. Although the flow statistics in the simulations are hemispherically symmetric (because the forcing and boundary conditions are), the instantaneous wind exhibits north-south asymmetries on large scales and ubiquitous variability on smaller scales. The large-scale variability has long timescales (~80 days), and the zonal-mean zonal wind is sensitive to the length of the time averaging: for timescales as long as the 500 days over which we averaged, the averages still exhibit hemispheric asymmetries (Fig. 6).

The vertically integrated eddy kinetic energy is 8.4 × 10$^5$ J m$^{-2}$ in the global mean. The instantaneous velocity fields exhibit substantial variability on relatively small scales (e.g., Fig. 7), and the kinetic energy spectrum decays only weakly from spherical wavenumber ~20 toward the roll-off near the grid scale owing to the subgrid-scale filter. However, the peak in velocity variance is at the largest scales (Fig. 8)—as suggested by the hemispherically asymmetric large-scale variability seen in Fig. 7 and in the animation.

### *3.4. Atmospheric stratification and energy transports*

Consistent with the scaling arguments presented above, horizontal variations in temperature are small in the free troposphere (above the ~750 hPa level, Fig. 9). This is reminiscent of Earth's tropics, where temperature variations are small because Coriolis accelerations are weak compared with inertial accelerations (e.g., Charney 1963; Sobel et al. 2001). Here, Coriolis accelerations are weak at all latitudes, and free-tropospheric horizontal temperature variations are small everywhere.

The thermal stratification on the day side in the simulation is moist adiabatic in the free troposphere within ~30° of the subsolar point. Farther away from the intense moist convec-

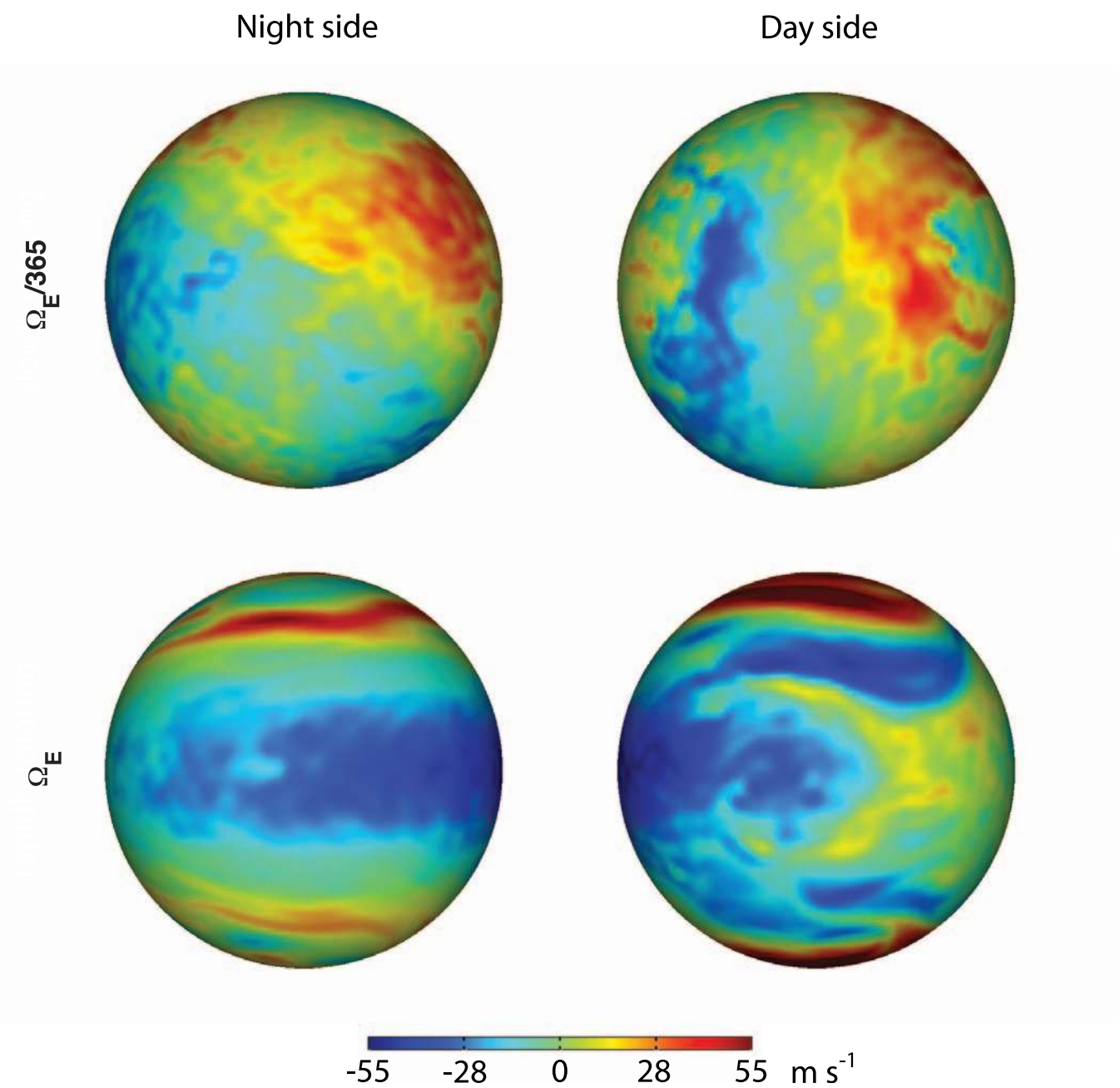


**Figure 7.** Instantaneous zonal wind on $\sigma = 0.28$ surface in the statistically steady state (on day 3900) of the two simulations. Animations are available at doi: 10.3894/JAMES.2010.2.13.S1 and doi: 10.3894/JAMES.2010.2.13.S2.

tion around the subsolar point, including on the night side of the planet, there are low-level temperature inversions (Fig. 9b), as in the simulations in Joshi et al. (1997). These regions have small optical thickness because of the low water vapor concentrations and therefore have strong radiative cooling to space from near the surface. The inversions arise because horizontal temperature gradients are constrained to be weak in the free troposphere, whereas near-surface air cools strongly radiatively, so that cool surface air underlies warm free-troposphere air.

The vertical and meridional integral of the zonal moist static energy flux divergence as a function of longitude is shown in Fig. 10 (dashed curves). Energy diverges on the day side and converges on the night side of the planet, reducing temperature contrasts. Near the subsolar point, there is substantial cancellation between the latent energy and dry static energy components of the moist static energy flux divergence as there is, for example, in Earth's Hadley circulation. As can be inferred from the minimal water vapor flux divergence on the night side (Fig. 2), the

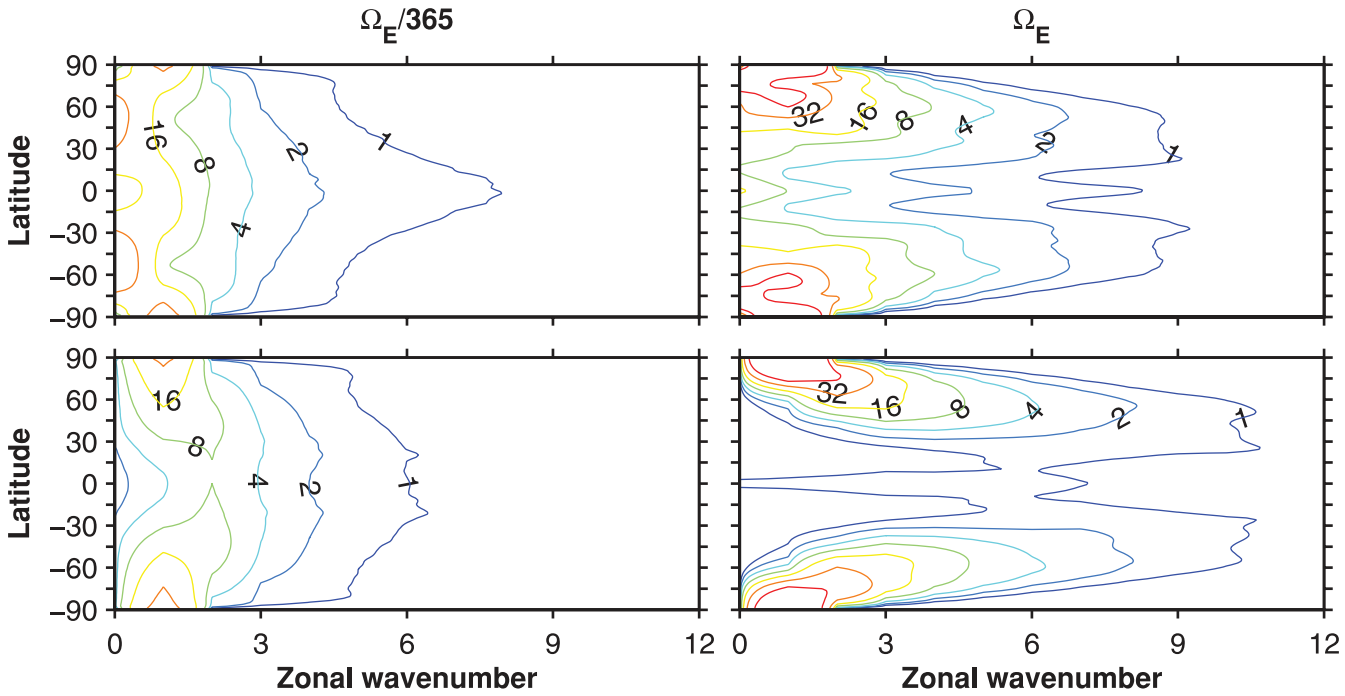


**Figure 8.** Spectrum of the mass-weighted, vertically averaged transient velocity variance for zonal (top row) and meridional (bottom row) wind components in the simulations with $\Omega_E/365$ (left) and $\Omega_E$ (right). Contours are shown at $2^0$, $2^1$, …, $2^6$ m$^2$ s$^{-2}$.

moist static energy flux divergence there is dominated by the dry static energy ($c_pT + gz$) component ( $\gtrsim$ 99% of the total).

## 4. Rapidly Rotating Simulation

In rapidly rotating atmospheres, the Rossby number in the extratropics is small, and geostrophic balance is the dominant balance in the horizontal momentum equations. In the zonal mean, zonal pressure gradients vanish, but meridional pressure gradients do not, so if the dominant momentum balance is geostrophic, winds are anisotropic with $\bar{U} > \bar{V}$, where $\overline{(\cdot)}$ denotes a zonal mean. Variations in the planetary vorticity with latitude, $\beta$, are central to vorticity mixing arguments (e.g., Rhines 1994; Held 2000), which can account for the generation of atmospheric zonal jets: When a Rossby wave packet stirs the atmosphere in a region bounded by a polar cap, high-vorticity fluid moves equatorward and low-vorticity fluid moves poleward. This reduces the vorticity in the polar

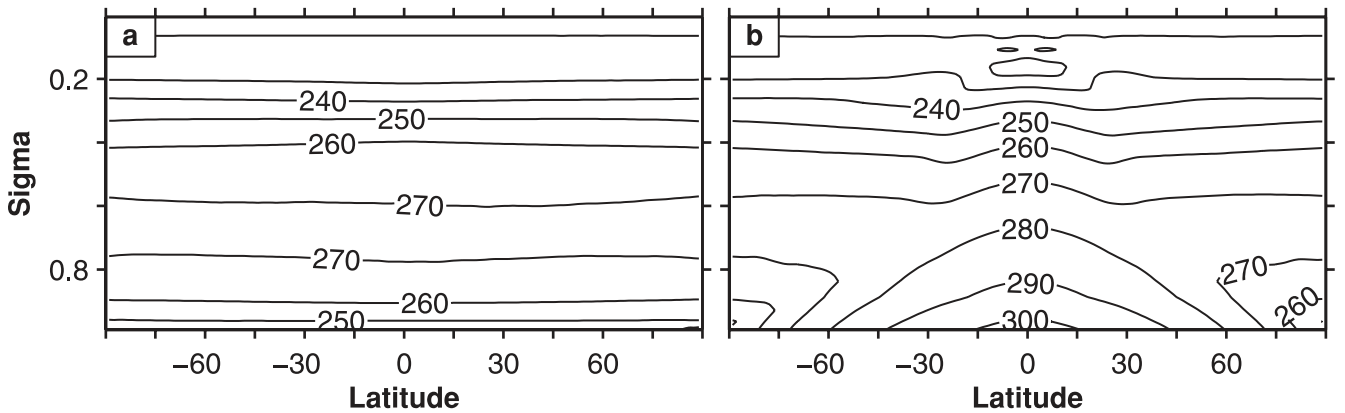


**Figure 9.** Temperature section of antisolar longitudes (a) and subsolar longitudes (b) of $\Omega_E/365$ simulation. Averages are taken over 10° of longitude. The contour interval is 10 K.

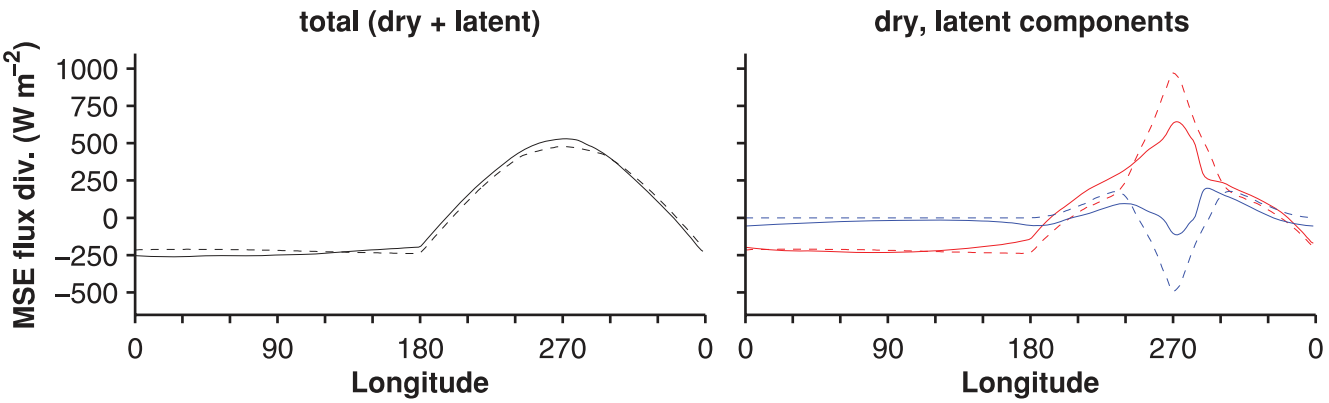


**Figure 10.** Left: Vertical and meridional integral of the divergence of the zonal moist static energy flux, *uh*. Right: Dry static energy (red) and latent energy (blue) components of moist static energy flux divergence. Dashed lines for $\Omega_E/365$ simulation and solid lines for $\Omega_E$ simulation.

cap. By Stokes' Theorem, the reduced vorticity in the polar cap means that the zonal wind at the latitude of the bounding cap decreases; if angular momentum is conserved, the zonal wind outside the polar cap increases. Irreversible vorticity mixing (wave-breaking or dissipation) is necessary to maintain the angular momentum fluxes in the time mean. Thus, the larger planetary vorticity gradients of the rapidly rotating planet allow zonal jets to form provided there is a source of wave activity that leads to vorticity stirring.

We return to the analysis of Charney (1963) to estimate temperature variations in the free atmosphere. For rapidly rotating planets, geostrophic balance holds in the horizontal momentum equations: $\delta p/(\rho L) \sim fU$. Combining the scaling from the momentum equation with the hydrostatic relation, the pressure, density, and (potential) temperature variations scale like the ratio of the Froude number to the Rossby number,

$$\frac{\delta p}{p} \sim \frac{\delta \rho}{\rho} \sim \frac{\delta \theta}{\theta} \sim \frac{fUL}{gH} = \frac{\mathrm{Fr}}{\mathrm{Ro}}. \qquad (4.1)$$

Where the Rossby number is small (in the extratropics), the temperature variations will be a factor of order inverse Rossby number ($\mathrm{Ro}^{-1} \sim 10$) larger than in the slowly rotating simulation for similar values of $U$, $g$, and $H$. Thus, we expect larger horizontal temperature and pressure variations away from the equator in the rapidly rotating simulation.

*4.1. Surface temperature and outgoing longwave radiation*

In the rapidly rotating simulation, the surface temperature on the day side of the planet is maximal off of the equator and does not bear a close resemblance to the insolation distribution; the night side of the planet has relatively warm regions in western high latitudes (Fig. 1). Compared to the slowly rotating simulation, the surface temperature is more substantially modified by the atmospheric circulation; however, the temperature contrasts between the day and night side are similar.

The outgoing longwave radiation of the rapidly rotating simulation has substantial variations (Fig. 1). Some of the structures in the surface temperature are echoed in the OLR distribution. Compared to the slowly rotating simulation, OLR variations have smaller spatial scales and occupy a wider range of values.

*4.2. Hydrological cycle*

Surface evaporation rates mimic the insolation distribution (Fig. 2). This is one of the most similar fields between the slowly and rapidly rotating simulations, as expected from the gross similarity in surface temperature and the smallness of the Bowen ratio at these temperatures (Fig. 3). This might not be the case if the model included the radiative effects of clouds since the amount of shortwave radiation reaching the surface would be shaped by variations in cloud albedo, which, in turn, depend on the atmospheric circulation.

Precipitation rates are large in a crescent-shaped region on the day side of the planet; the night side of the planet generally has small but nonzero precipitation rates (Fig. 2). The evaporation minus precipitation field has substantial structure: there are large amplitude changes from the convergence zones ($P > E$) to nearby areas of significant net drying ($E > P$). Comparing the slowly and rapidly rotating simulations shows that precipitation and $E - P$ on the night side of the planet are sensitive to the atmospheric circulation.

An interesting aspect of the climate is that the precipitation maximum (near ∼15° latitude) is not co-located with the off-equatorial surface temperature maximum (near ∼40° latitude). The simulation provides an example of precipitation and deep convection that are not locally thermodynamically controlled: the precipitation is not maximum where the surface temperature is maximum; the

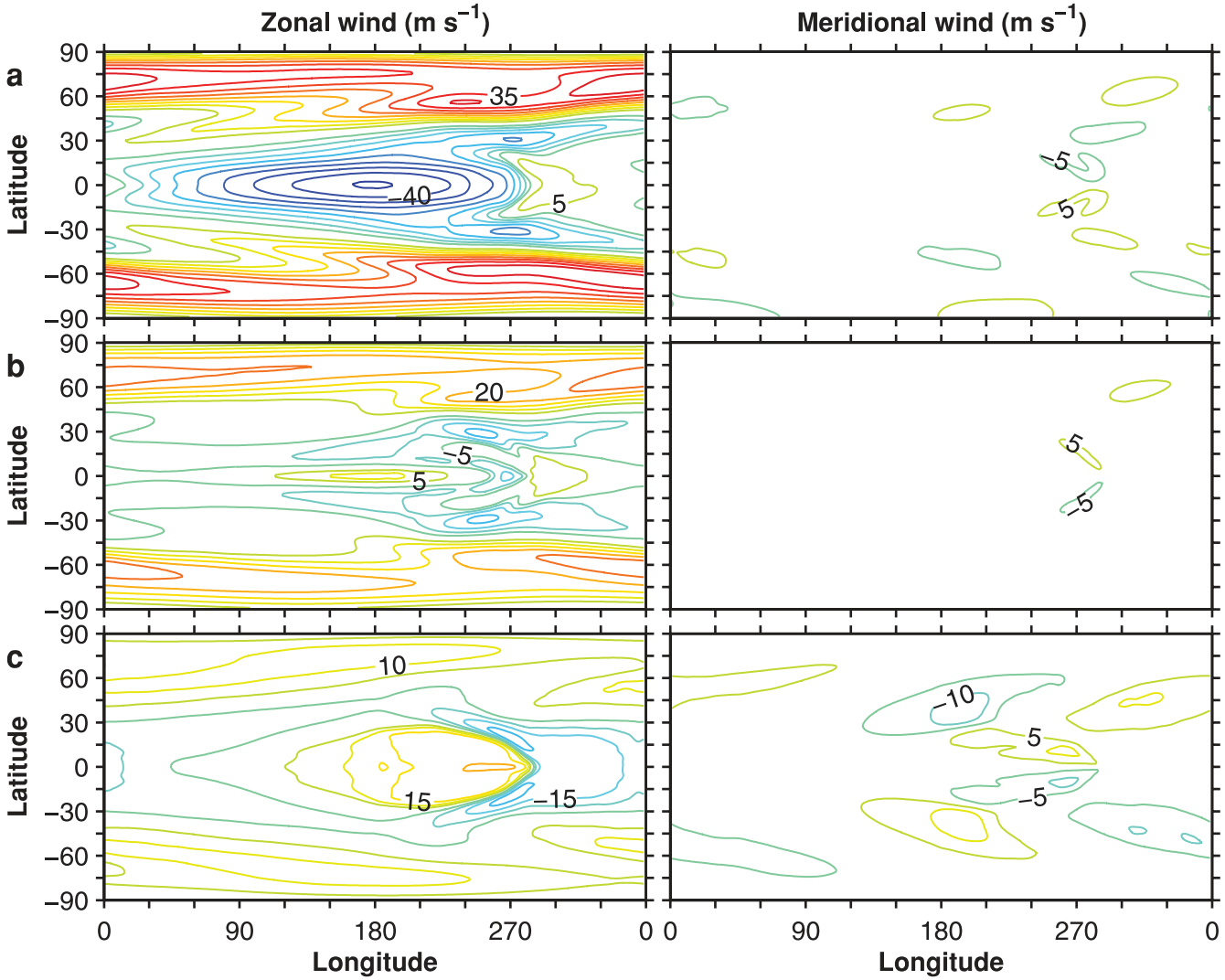


**Figure 11.** Zonal wind (left) and meridional wind (right) of $\Omega_E$ simulation on the $\sigma = 0.28$ (a), 0.54 (b), and 1.0 (c) surfaces. The contour interval is 5 m $s^{-1}$, and the zero contour is not shown.

column static stability (e.g., Fig. 13), and therefore the convective available potential energy, are not markedly different between the maxima in precipitation and temperature. However, if the surface climate is examined latitude-by-latitude instead of examining the global maxima, the region of large precipitation is close to the maximum surface temperature (as well as surface temperature curvature) at a given latitude. The structure of the surface winds, discussed next, and the associated moisture convergence are key for determining where precipitation is large. Sobel (2007) provides a review of these two classes of theories for tropical precipitation (thermodynamic control vs. momentum control) and the somewhat inconclusive evidence of which class of theory better accounts for Earth observations.

The global precipitation is ~10% larger in the rapidly rotating simulation than in the slowly rotating simulation. This suggests that radiative-convective equilibrium cannot completely describe the strength of the hydrological cycle.

### *4.3. General circulation of the atmosphere*

In the rapidly rotating simulation, the atmospheric circulation has several prominent features: there are westerly jets in high (~65°) latitudes, the mid-tropospheric zonal wind exhibits equatorial superrotation, and the surface winds converge in a crescent-shaped region near the subsolar point (Fig. 11). The equatorial superrotation and westerly jets are evident in the zonal-mean zonal wind (Fig. 6).

The existence of the high-latitude jets can be understood from the temperature field and eddy angular momentum flux convergence (Figs. 13 and 6). There are large meridional temperature gradients, which give rise to zonal wind shear by thermal wind balance and provide available poten-

tial energy for baroclinic eddies that transport angular momentum into the jets. In the vertical average, the eddy angular momentum transport into an atmospheric column is balanced by surface stress (provided the Rossby number is small), so surface westerlies appear underneath high-latitude regions of angular momentum flux convergence.

The equatorial superrotation is a consequence of angular momentum flux convergence (Fig. 6). Saravanan (1993) and Suarez and Duffy (1992) describe the emergence of superrotation generated by large-scale, zonally asymmetric heating anomalies in the tropics. As in their idealized models, the zonal asymmetry in the low-latitude heating (in our simulation, provided by insolation) generates a stationary Rossby wave. Consistent with a stationary wave source, in the rapidly rotating simulation, the horizontal eddy angular momentum flux convergence in low latitudes is dominated by the stationary eddy component. This aspect of the simulation is sensitive to horizontal resolution and the subgrid-scale filter. With higher resolution or weaker filtering, the superrotation generally extends higher into the troposphere and has a larger maximum value.

There is a crescent-shaped region where the surface zonal wind is converging. This is where the precipitation (Fig. 2) and upward vertical velocity (Fig. 5) are largest. The horizontal scale of the convergence zone is similar to the equatorial Rossby radius, $(c/\beta)^{1/2}$, where $\beta$ is the gradient of planetary vorticity and $c$ is the gravity wave speed. If moisture effects are neglected, the gravity wave speed is estimated using a characteristic tropospheric value for the Brunt-Väisälä frequency on the day side of the planet, the equatorial Rossby radius corresponds to $\sim 10^\circ$ latitude, which is of the same order as the scale of the convergence zone. The surface zonal wind can be qualitatively understood as the equatorially-trapped wave response to stationary heating: equatorial Kelvin waves propagate to the east of the heating and generate easterlies; equatorial Rossby waves propagate to the west of the heating and generate westerlies (Gill 1980).

The shape of the zero zonal wind line and its horizontal scale are similar to those of the Gill (1980) model, which describes the response of damped, linear shallow-water waves to a prescribed heat/mass source. For the prescribed heat source in the original Gill model, the crescent-shape zero zonal wind line extends over $\sim 2$ Rossby radii and, as in the GCM simulation, is displaced to the east of the heating maximum on the equator.

A complicating factor in the analogy between the GCM's low-latitude surface winds and those of the Gill model is that the heating is prescribed in the Gill model, while it interacts with the flow in the GCM. As previously mentioned, the precipitation is strongly shaped by the winds. To see if the analogy between the winds in the GCM and in the Gill model breaks down because of the more complex structure of the latent heating, we force a variant of the Gill model with the GCM's precipitation field following the formulation of Neelin (1988) (see Appendix for details). The results of this calculation are compared with the GCM output in Fig. 12. The direction, large-scale structure, and, in the case of the zonal component, magnitude of the mass fluxes are similar between the GCM and precipitation-forced Gill model, though it is clear that there are quantitative differences. Better quantitative agreement particularly in the meridional component could be achieved by using anisotropic damping (different damping coefficients in the zonal and meridional direction) in the Gill model, as is common in studies of Earth's atmosphere (e.g., Stevens et al. 2002).

In contrast to the zonal wind, which has larger magnitude, the meridional wind is diverging at the surface and converging aloft near the subsolar point (right panel of Fig. 11a,c). As discussed by Gill (1980), the reasons for this lie in the vorticity balance: for a Sverdrup vorticity balance, the vortex stretching caused by the overall convergence near the surface near the equator must be balanced by poleward motion, toward higher planetary vorticity, and vice versa at higher levels; hence, the meridional wind is poleward near the surface and equatorward aloft.

The Eulerian mean mass streamfunction (Fig. 6) has the opposite sense as Earth's Hadley cells: in the zonal mean, there is descent at the equator, poleward flow near the surface, ascent near 15°, and equatorward flow near the surface and in the mid-troposphere. If the dominant balance in the zonal momentum equation is between Coriolis acceleration and eddy angular momentum flux divergence, $-f\bar{v} \sim \partial_y \overline{u'v'}$ (i.e., small local Rossby number as defined in Walker and Schneider (2006)), then the angular momentum flux convergence that establishes the superrotating zonal wind also leads to equatorward mean meridional wind in the free troposphere, as in Earth's Ferrel cells (e.g., Held 2000). This can lead to a dynamical feedback that enhances superrotation (Schneider and Liu 2009): as superrotation emerges, the mean meridional circulation can change direction with a concomitant change in the direction of mean-flow angular momentum fluxes (changing from exporting angular momentum from the deep tropics to importing it), which enhances the superrotation.

The instantaneous, upper tropospheric zonal wind in the rapidly rotating simulation is shown in Fig. 7, and a corresponding animation is available at doi: 10.3894/JAMES.2010.2.13.S2. The large-scale features of the general circulation such as the high-latitude jets and divergent zonal wind in the tropical upper troposphere are clear in the instantaneous winds. The eddies in the animation generally have larger spatial scales and longer timescales than in the corresponding slowly rotating animation.

The vertically and globally integrated eddy kinetic energy is $1.0 \times 10^6$ J m$^{-2}$. This is about 20% larger than in the slowly rotating case. The eddy kinetic energy spectrum has a typical $n^{-3}$ shape in spherical wavenumber $n$, up to the smallest resolved wavenumber. But the integrated eddy kinetic energy hides an important difference in synoptic

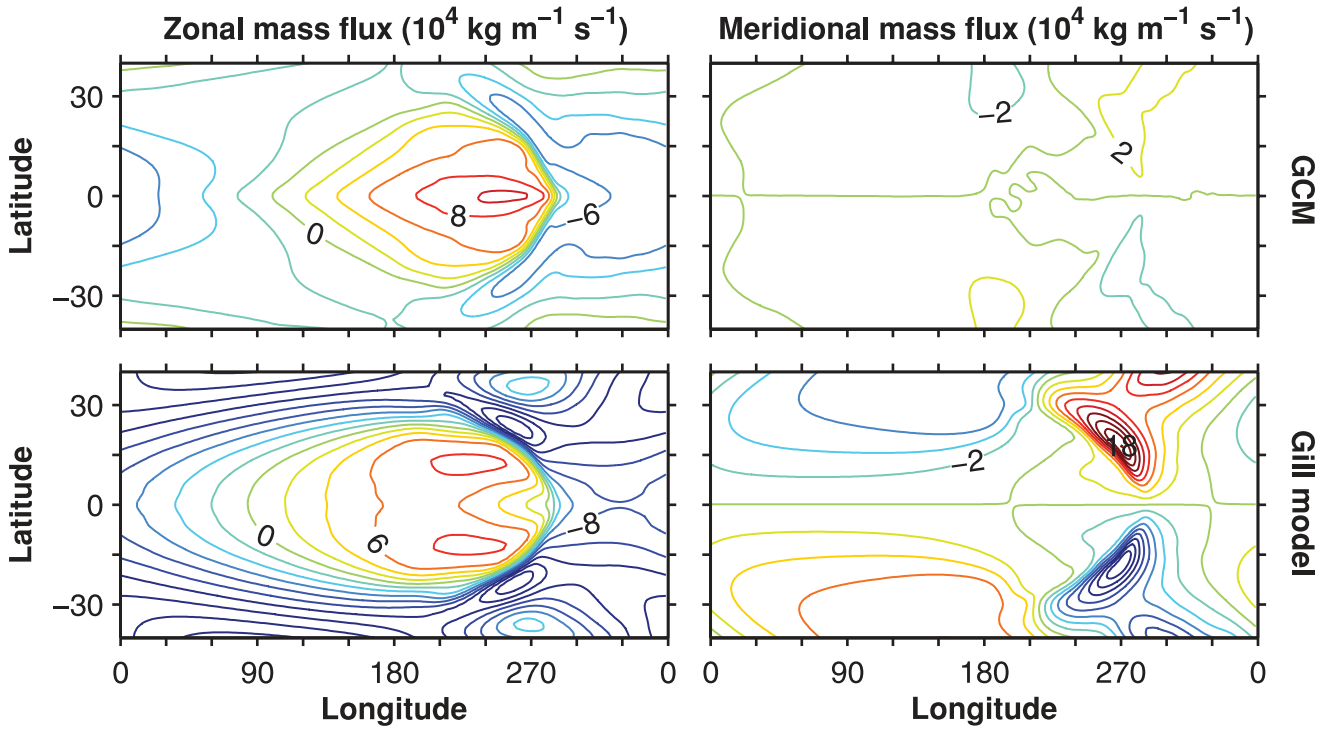


**Figure 12.** Zonal (left column) and meridional (right column) near-surface mass fluxes for the GCM (top row, averaged between the surface and $\sigma = 0.73$ model level) and the Gill model forced by the GCM's precipitation (bottom row, see Appendix for Gill model equations and parameters). The contour interval is $2 \times 10^4$ kg m$^{-1}$ s$^{-1}$.

variability between the rapidly and slowly rotating simulations: in the extratropics, for zonal wavenumbers between ~3–6, the rapidly rotating simulation has a factor of 2–3 times more velocity variance (Fig. 8) than the slowly rotating simulation.

*4.4. Atmospheric stratification and energy transports*

The tropospheric temperature distribution on the day side of the planet (Fig. 13) resembles the surface temperature distribution: the temperature field has a local maximum near ~40° latitude and is relatively uniform up to high latitudes (up to ~50°). In the free troposphere on the day side, the lapse rates are close to the moist adiabatic lapse rate, computed using the local temperature and pressure, over a region roughly within the 300 K contour of the surface temperature. Note that 300 K does not have a particular physical significance, e.g., as a deep convection threshold—we are simply using it to describe a feature of the

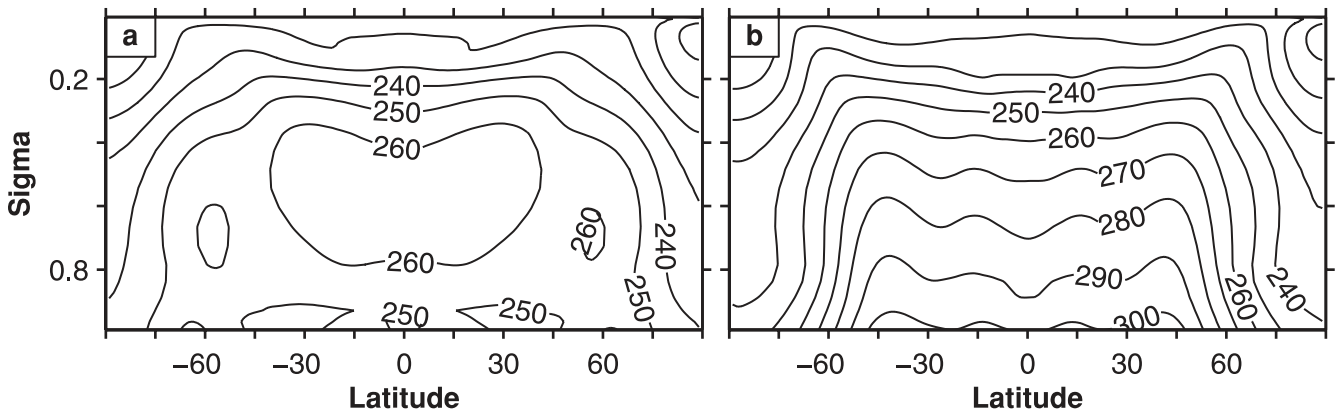


**Figure 13.** Temperature section of antisolar longitudes (a) and subsolar longitudes (b) in $\Omega_E$ simulation. Averages are taken over 10° of longitude. The contour interval is 10 K.

simulation. There is a local minimum of temperature on the equator which may be related to the downward vertical velocity there (Fig. 5). In low latitudes, there is a near-surface inversion on the night side of the rapidly rotating simulation that, as in the slowly rotating simulation, is the result of weak temperature gradients in the free troposphere and the substantial radiative cooling owing to the small optical thickness of the atmosphere.

As in the slowly rotating simulation, the moist static energy flux diverges on the day side and converges on night side of the planet (solid curves in Fig. 10); there is substantial cancellation between the dry static energy flux and the latent energy flux divergence near the subsolar point. Though the hydrological cycle is more active on the night side of the rapidly rotating simulation than in the slowly rotating simulation, the dry static energy component still dominates ( $\gtrsim$ 80% of total) the moist static energy advection on the night side of the planet.

The two simulations are more similar in this respect than might have been anticipated given the differences in their flow characteristics, although there are regional differences that are obscured by averaging over latitude. The broad similarities can be understood by considering the moist static energy budget. In the time mean, denoted by $[\cdot]$, neglecting kinetic energy fluxes and diffusive processes within the atmosphere, the mass-weighted vertical integral $\langle\cdot\rangle$ of the moist static energy flux divergence is balanced by surface energy fluxes $F_s$ and radiative tendencies $Q_{rad}$,

$$\nabla\cdot\langle[\mathbf{u}h]\rangle = [F_s] + [Q_{rad}]. \tag{4.2}$$

As a result of the gross similarity of the two simulations in evaporation and low-latitude stratification (in part due to the smaller dynamical role that rotation plays near the equator), and hence the gross similarity in radiative cooling, the divergence of the moist static energy flux is also similar, at least in low latitudes and in the meridional mean. Locally in the extratropics, however, considering the sources and sinks of moist static energy does not provide a useful constraint because the stratification is dynamically determined and not moist adiabatic (e.g., Schneider 2007), and there can be geostrophically balanced temperature gradients in rapidly rotating atmospheres. As a consequence, the radiative cooling, through dynamical influences on temperature, is determined by the flow, so the moist static energy flux divergence will generally depend on the rotation rate. Indeed, the warm regions on the night side of the rapidly rotating simulation have larger moist static energy flux divergence than the corresponding regions in the slowly rotating simulation.

## 5. Systematic Variation of Rotation Rate

### 5.1. Equatorial superrotation

In the rapidly rotating simulation, the mid-tropospheric zonal-mean zonal winds near the equator are weakly superrotating. In the slowly rotating simulation, they are also superrotating, but even more weakly so. Given that equatorial superrotation generally occurs even with zonally symmetric heating when planetary rotation rates are sufficiently low ($\Omega \lesssim \Omega_E/4$ for the otherwise Earth-like planets in Walker and Schneider (2006)), one may suspect that the zonal-mean zonal winds are more strongly superrotating at intermediate planetary rotation rates.

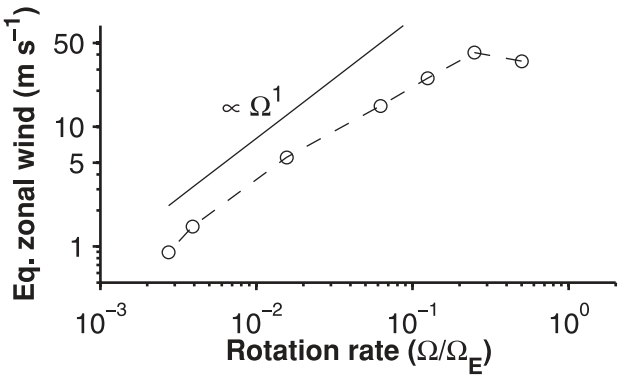


**Figure 14.** Barotropic equatorial zonal-mean zonal wind vs. rotation rate averaged within 3° of latitude of the equator. Solid line shows power law with exponent +1. For $\Omega = \Omega_E$, the zonal wind is $-7.1$ m s$^{-1}$ and hence is not shown.

Figure 14 shows the barotropic (mass-weighted vertical average) equatorial zonal-mean zonal wind as the rotation rate is varied. Simulated rotation rate values are $\Omega$ = (1, 1/2, 1/4, 1/8, 1/16, 1/64, 1/256, 1/365) $\Omega_E$. The strength of the equatorial superrotation indeed is maximal for intermediate rotation rates ($\Omega \approx \Omega_E/4$).

The increase with rotation rate in the strength of equatorial superrotation for low values of $\Omega$ can be qualitatively understood from the angular momentum balance and the way eddies enter it. The angular momentum balance near the equator is generally dominated by the angular momentum flux convergence by stationary eddies and by the zonal-mean flow; angular momentum fluxes associated with transient eddies are weaker. The stationary eddy angular momentum flux convergence increases with rotation rate, with a somewhat weaker than linear dependence on rotation rate; it has a maximum at intermediate rotation rates ($\Omega \approx \Omega_E/4$). This is a consequence, in part, of the increase in vortex stretching and vorticity advection by the divergent flow with increasing rotation rate: The stationary Rossby waves giving rise to the angular momentum flux are generated by vortex stretching in divergent flow or by vorticity advection by the divergent flow, which is generated at upper levels by the heating around the subsolar point (Sardeshmukh and Hoskins 1988). The eddy angular momentum flux convergence is equal to the rate at which Rossby wave activity is generated (e.g., Schneider and Liu 2009).

To understand the full behavior of the superrotation over the range of rotation rates, one must also understand the angular momentum flux divergence by the zonal-mean flow;

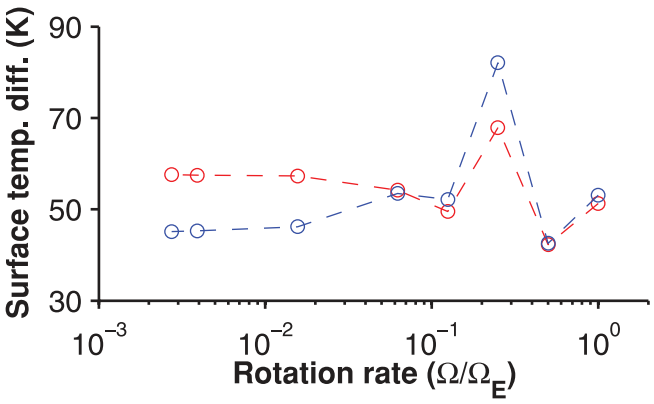


**Figure 15.** Surface temperature contrast between the day side and the night side vs. rotation rate. Averages are taken over 10° of longitude centered at the substellar and antistellar points and between −30° and 30° of latitude (red) and between 30° and 60° of latitude (blue).

however, these changes are not simple as the strength of the Hadley circulation depends on rotation rate and the character of the angular momentum balance changes with rotation rate—the local Rossby number decreases as rotation rate increases. Such changes in the Hadley circulation likely play a role in the decrease in the strength of equatorial superrotation as the rotation rate increases beyond $\sim\Omega_E/4$. Additionally, changes in the vertical shear contribute to changes in the strength of equatorial superrotation; in the slowly rotating limit, the shear is no longer related to the temperature field by gradient wind balance.

We have also performed simulations with zonally symmetric insolation that are otherwise identical to those in Fig. 14. While there is equatorial superrotation, it is substantially weaker: $\sim$5 m s$^{-1}$ compared to $\sim$25 m s$^{-1}$ at intermediate rotation rates. This suggests qualitative differences in the atmospheric circulation when there is zonally symmetric forcing compared to zonally asymmetric forcing and provides an additional demonstration of the central role stationary eddies play in the superrotation of the tidally locked simulations.

*5.2. Day-side to night-side temperature contrast*

Figure 15 shows the day-side to night-side surface temperature contrast in the simulations with different rotation rates. As suggested by the slowly and rapidly rotating simulations examined in detail above, the surface temperature contrast is does not vary strongly with changes in rotation rate: it is $\sim$50 K over the range of simulations, with variations of about $\pm$20 K depending on the rotation rate. The variations suggest that quantitative estimates of surface temperature differences must account for circulation changes.

## 6. Conclusions

We have examined the dynamics of tidally locked, Earth-like planets. The dynamical regime of the atmosphere depends on the planet rotation rate, as anticipated from scaling arguments. The simulations demonstrate the importance of the atmospheric circulation in determining the surface climate. For example, the difference between the precipitation distributions in the slowly and rapidly rotating simulations clearly shows the dependence of the hydrological cycle on the circulation of the atmosphere. Interestingly, some aspects of the simulated climate are not sensitive to the planet's rotation rate. In particular, the temperature contrast between the day and night side and evaporation rates are similar between the slowly and rapidly rotating simulations.

The general circulation of the slowly rotating atmosphere features global-scale, thermodynamically-direct, divergent circulations with ascending motion at the subsolar point and descending motion elsewhere. In contrast, the general circulation of the rapidly rotating atmosphere features extratropical jets that owe their existence to rotational (Rossby) waves, and tropical surface winds that are the result of stationary equatorial (Rossby and Kelvin) waves. The isotropy of the winds in the slowly rotating regime and the anisotropy of the winds in the rapidly rotating regime are expected from the dominant balance of the horizontal momentum equations. Expectations for the free-atmospheric pressure and temperature gradients based on scale analysis were realized in the simulations of the different circulations regimes: temperature gradients are weak where Coriolis accelerations are weak (in low latitudes of the rapidly rotating atmosphere and globally in the slowly rotating atmosphere) and larger where Coriolis accelerations are dynamically important (in the extratropics of the rapidly rotating atmosphere).

The series of simulations with varying rotation rates demonstrates that the degree of equatorial superrotation varies non-monotonically. A full explanation for the dependence of equatorial superrotation on the rotation rate remains an open question. In contrast, the surface temperature contrast between the day side and the night side is approximately 50 K over the range of rotation rates.

While many aspects of the simulations can be explained by general circulation theories for Earth and Earth-like atmospheres, there remain quantitative questions that require more systematic experimentation than we have attempted here. For example, the dependence of the surface climate on the solar constant may be different from simulations with Earth-like insolation because of the differences in stratification.

**Acknowledgments:** Timothy Merlis was supported by a National Defense Science and Engineering Graduate fellowship and a National Science Foundation Graduate Research fellowship. We thank Dorian Abbot and Sonja Graves for providing modifications to the GCM code and Simona Bordoni, Ian Eisenman, Andy Ingersoll, Yohai Kaspi, and two anonymous reviewers for comments on the manuscript. The simulations were performed on Caltech's Division of

**Table 1.** Gill model constants and their values.

| Constant | Value |
|---|---|
| c | 50 m $s^{-1}$ |
| $\beta$ | 2.22 $\times$ $10^{-11}$ $m^{-1}$ $s^{-1}$ |
| $\epsilon_m$ | (1 day)$^{-1}$ |
| $\epsilon_T$ | (20 day)$^{-1}$ |
| a | 7.14 $\times$ $10^5$ J $kg^{-1}$ |

Geological and Planetary Sciences Dell cluster. The program code for the simulations, based on the Flexible Modeling System of the Geophysical Fluid Dynamics Laboratory, and the simulation results themselves are available from the authors upon request.

## 7. Appendix: Gill Model Forced by Precipitation

We use the formulation for a Gill model forced by precipitation (Neelin 1988), as opposed to the standard mass sink. The model equations are

$$-f\tilde{v} = -\partial_x\tilde{\phi} - \varepsilon_m\tilde{u} \tag{7.1}$$

$$f\tilde{u} = -\partial_y\tilde{\phi} - \varepsilon_m\tilde{v} \tag{7.2}$$

$$c^2\left(\partial_x\tilde{u} + \partial_y\tilde{v}\right) = -aP - \varepsilon_T\tilde{\phi}, \tag{7.3}$$

where $a = LR/c_p$ is the combination of the latent heat of vaporization, gas constant, and heat capacity at constant pressure that results from converting the precipitation rate to a temperature tendency in the thermodynamic equation and approximating Newtonian cooling by geopotential damping, $\epsilon_m$ is the Rayleigh drag coefficient of the momentum equations, $\epsilon_T$ is the damping coefficient for the geopotential, other variables have their standard meanings (e.g. $P$ is precipitation), and $\widetilde{(\cdot)} = \int_{p_b}^{p_s} (\cdot)\, dp/g$ is the mass-weighted vertical integral over the boundary layer ($p_b$ is the pressure at the top of the boundary layer). We use fairly standard values for the constants (Table 1). The qualitative aspects of the solutions that we discuss are not sensitive to these choices.

The three equations can be combined into a single equation for $\tilde{v}$:

$$\left[-\varepsilon_T\left(\varepsilon_m^2 + \beta^2 y^2\right)/c^2 + \varepsilon_m\left(\partial_{xx} + \partial_{yy}\right) + \beta\,\partial_x\right]\tilde{v} = -\left(\varepsilon_m\partial_y - \beta y\,\partial_x\right)aP/c^2, \tag{7.4}$$

where $\beta$-plane geometry ($f = \beta y$) has been assumed. The boundary value problem for $\tilde{v}$ is discretized by Fourier transforming in the x-direction and finite differencing in the y-direction. It is solved using the GCM's climatological precipitation field (Fig. 2) on the right-hand side.

## References


Charbonneau, D., and Coauthors, 2009: A super-Earth transiting a nearby low-mass star. *Nature*, **462**, 891–894, doi: 10.1038/nature08679.

Charbonneau, D., T. M. Brown, D. W. Latham, and M. Mayor, 2000: Detection of planetary transits across a Sun-like star. *Astrophys. J.*, **529**, L45–L48, doi: 10.1086/312457.

Charney, J. G., 1963: A note on large-scale motions in the Tropics. *J. Atmos. Sci.*, **20**, 607–609, doi: 10.1175/1520-0469(1963)020<0607:ANOLSM>2.0.CO;2.

Frierson, D. M. W., 2007: The dynamics of idealized convection schemes and their effect on the zonally averaged tropical circulation. *J. Atmos. Sci.*, **64**, 1959–1976, doi: 10.1175/JAS3935.1.

Frierson, D. M. W., I. M. Held, and P. Zurita-Gotor, 2006: A gray-radiation aquaplanet moist GCM. Part I: Static stability and eddy scale. *J. Atmos. Sci.*, **63**, 2548–2566, doi: 10.1175/JAS3753.1.

Gill, A. E., 1980: Some simple solutions for heat-induced tropical circulation. *Quart. J. Roy. Meteor. Soc.*, **106**, 447–462, doi: 10.1002/qj.49710644905.

Hartmann, D., 1994: *Global Physical Climatology*. Academic Press, 411 pp.

Held, I. M., 2000: The general circulation of the atmosphere. *Proc. Program in Geophysical Fluid Dynamics*, Woods Hole Oceanographic Institution, Woods Hole, MA. URL https://darchive.mblwhoilibrary.org/handle/1912/15.

Held, I. M., and A. Y. Hou, 1980: Nonlinear axially symmetric circulations in a nearly inviscid atmosphere. *J. Atmos. Sci.*, **37**, 515–533, doi: 10.1175/1520-0469(1980)037<0515:NASCIA>2.0.CO;2.

Hide, R., 1969: Dynamics of the atmospheres of the major planets with an appendix on the viscous boundary layer at the rigid bounding surface of an electrically-conducting rotating fluid in the presence of a magnetic field. *J. Atmos. Sci.*, **26**, 841–853, doi: 10.1175/1520-0469(1969)026<0841:DOTAOT>2.0.CO;2.

Hubbard, W. B., 1984: *Planetary Interiors*. Van Nostrand Reinhold Co., 334 pp.

Joshi, M., 2003: Climate model studies of synchronously rotating planets. *Astrobiology*, **3**, 415–427, doi: 10.1089/153110703769016488.

Joshi, M. M., R. M. Haberle, and R. T. Reynolds, 1997: Simulations of the atmospheres of synchronously rotating terrestrial planets orbiting M Dwarfs: Conditions for atmospheric collapse and the implications for habitability. *Icarus*, **129**, 450–465, doi: 10.1006/icar.1997.5793.

Neelin, J. D., 1988: A simple model for surface stress and lowlevel flow in the tropical atmosphere driven by prescribed heating. *Quart. J. Roy. Meteor. Soc.*, **114**, 747–770, doi: 10.1002/qj.49711448110.

O'Gorman, P. A., and T. Schneider, 2008: The hydrological cycle over a wide range of climates simulated with an

idealized GCM. *J. Climate*, **21**, 3815–3832, doi: 10.1175/2007JCLI2065.1.

Pierrehumbert, R. T., 2002: The hydrologic cycle in deep-time climate problems. *Nature*, **419**, 191–198, doi: 10.1038/nature01088.

Pierrehumbert, R. T., 2010: *Principles of Planetary Climate*. Cambridge University Press, 688 pp.

Rhines, P. B., 1994: Jets. *Chaos*, **4**, 313–339, doi: 10.1063/1.166011.

Saravanan, R., 1993: Equatorial superrotation and maintenance of the general circulation in two-level models. *J. Atmos. Sci.*, **50**, 1211–1227, doi: 10.1175/1520-0469(1993)050<1211:ESAMOT>2.0.CO;2.

Sardeshmukh, P. D., and B. J. Hoskins, 1988: The generation of global rotational flow by steady idealized tropical divergence. *J. Atmos. Sci.*, **45**, 1228–1251, doi: 10.1175/1520-0469(1988)045<1228:TGOGRF>2.0.CO;2.

Schneider, E. K., 1977: Axially symmetric steady-state models of the basic state for instability and climate studies. Part II. Nonlinear calculations. *J. Atmos. Sci.*, **34**, 280–296, doi: 10.1175/1520-0469(1977)034<0280:ASSSMO>2.0.CO;2.

Schneider, T., 2006: The general circulation of the atmosphere. *Ann. Rev. Earth Planet. Sci.*, **34**, 655–688, doi: 10.1146/annurev.earth.34.031405.125144.

Schneider, T., 2007: The thermal stratification of the extratropical troposphere. T. Schneider and A. H. Sobel, Eds., *The Global Circulation of the Atmosphere*, Princeton University Press, 47–77.

Schneider, T., and J. J. Liu, 2009: Formation of jets and equatorial superrotation on Jupiter. *J. Atmos. Sci.*, **66**, 579–601, doi: 10.1175/2008JAS2798.1.

Showman, A. P., J. Y.-K. Cho, and K. Menou, 2010: Atmospheric circulation of extrasolar planets. S. Seager, Ed., *Exoplanets*, University of Arizona Press.

Smith, K. S., G. Boccaletti, C. C. Henning, I. N. Marinov, C. Y. Tam, I. M. Held, and G. K. Vallis, 2002: Turbulent diffusion in the geostrophic inverse energy cascade. *J. Fluid Mech.*, **469**, 13–48, doi: 10.1017/S0022112002001763.

Sobel, A. H., 2007: Simple models of ensemble-averaged tropical precipitation and surface wind, given the sea surface temperature. T. Schneider and A. H. Sobel, Eds., *The Global Circulation of the Atmosphere*, Princeton University Press, 219–251.

Sobel, A. H., J. Nilsson, and L. M. Polvani, 2001: The weak temperature gradient approximation and balanced tropical moisture waves. *J. Atmos. Sci.*, **58**, 3650–3665, doi: 10.1175/1520-0469(2001)058<3650:TWTGAA>2.0.CO;2.

Stevens, B., J. Duan, J. C. McWilliams, M. Münnich, and J. D. Neelin, 2002: Entrainment, Rayleigh friction, and boundary layer winds over the tropical Pacific. *J. Climate*, **15**, 30–44, doi: 10.1175/1520-0442(2002)015<0030:ERFABL>2.0.CO;2.

Suarez, M. J., and D. G. Duffy, 1992: Terrestrial superrotation: A bifurcation of the general circulation. *J. Atmos. Sci.*, **49**, 1541–1554, doi: 10.1175/1520-0469(1992)049<1541:TSABOT>2.0.CO;2.

Thuburn, J., and G. C. Craig, 2000: Stratospheric influence on tropopause height: The radiative constraint. *J. Atmos. Sci.*, **57**, 17–28, doi: 10.1175/1520-0469(2000)057<0017:SIOTHT>2.0.CO;2.

Trenberth, K. E., J. T. Fasullo, and J. Kiehl, 2009: Earth's global energy budget. *Bull. Amer. Meteor. Soc.*, **90**, 311–323, doi: 10.1175/2008BAMS2634.1.

Walker, C. C., and T. Schneider, 2006: Eddy influences on Hadley circulations: Simulations with an idealized GCM. *J. Atmos. Sci.*, **63**, 3333–3350, doi: 10.1175/JAS3821.1.

Williams, G. P., 1988: The dynamical range of global circulations — I. *Climate Dyn.*, **2**, 205–260, doi: 10.1007/BF01371320.